ARTICLE

Two Step Chemical Vapor Deposition of $In_2Se_3/MoSe_2$ van der Waals Heterostructures

Yu-lin Chen[a], Ming-ling Li[b], Yi-ming Wu[b], Si-jia Li[a], Yue Lin[a], Dong-xue Du[b], Huai-yi Ding[a], Nan Pan[a,b,c,d*], Xiao-ping Wang[a,b,c,d*]

a. Hefei National Laboratory for Physical Sciences at the Microscale, University of Science and Technology of China, Hefei 230026, China
b. Department of physics, University of Science and Technology of China, Hefei 230026, China
c. Synergetic Innovation Center of Quantum Information & Quantum Physics, University of Science and Technology of China, Hefei 230026, China
d. Key Laboratory of Strongly-Coupled Quantum Matter Physics, Chinese Academy of Sciences, School of Physical Sciences, University of Science and Technology of China, Hefei 230026, China

(Dated: Received on April 5, 2017; Accepted on April 19, 2017)

Two-dimensional transition metal dichalcogenides heterostructures have stimulated wide interest not only for the fundamental research, but also for the application of next generation electronic and optoelectronic devices. Herein, we report a successful two-step chemical vapor deposition strategy to construct vertically stacked van der Waals epitaxial $In_2Se_3/MoSe_2$ heterostructures. Transmission electron microscopy characterization reveals clearly that the In_2Se_3 has well-aligned lattice orientation with the substrate of monolayer $MoSe_2$. Due to the interaction between the In_2Se_3 and $MoSe_2$ layers, the heterostructure shows the quenching and red-shift of photoluminescence. Moreover, the current rectification behavior and photovoltaic effect can be observed from the heterostructure, which is attributed to the unique band structure alignment of the heterostructure, and is further confirmed by Kevin probe force microscopy measurement. The synthesis approach via van der Waals epitaxy in this work can expand the way to fabricate a variety of two-dimensional heterostructures for potential applications in electronic and optoelectronic devices.

Key words: van der Waals heterostructures, Chemical vapor deposition, $In_2Se_3/MoSe_2$, Kevin probe force microscopy, n^+-n junction

I. INTRODUCTION

Two-dimensional (2D) layered semiconductors, including transition metal dichalcogenides (TMDs) (MX_2, where M=transition metals such as Mo or W, and X=S, Se, or Te) and III−VI group layered chalcogenides (MX or M_2X_3, where M=Ga or In, and X=S, Se, or Te), have attracted broad attention for applications of next-generation electronic and optoelectronic devices [1−4]. Particularly, it is of tremendous significance to form novel 2D heterostructures for not only fundamental research, such as long-lived interlayer excitons in $MoSe_2/WSe_2$ heterostructure owing to type-II junction band alignment and ultrafast charge separation [5−7], but also many device applications including photovoltaics, light-emitting diodes, and photodetectors [8−10]. Although stacking different 2D materials by using mechanical transfer techniques is quite convenient and efficient, the stacked orientation cannot be precisely controlled, and the interface is often contaminated [11, 12]. In contrast, direct van der Waals (vdW) epitaxy can realize not only vertical heterostructures with well-defined interlayer orientations and clean interfaces by vertically stacking multiple 2D materials layer-by-layer [5−7, 13−19], but also lateral heterojunctions with seamless connections achieved by successive in-plane epitaxial growth of a second material from the edge of an existing crystal [20−28]. Till now, most of previous studies focused on heterostructures with two different MX_2, such as WS_2/WSe_2 [20], $WSe_2/MoSe_2$ [21, 24], WS_2/MoS_2 [22, 23], and WSe_2/MoS_2 [25], and many new physical phenomena and functionalities have been demonstrated. It is of great significance to explore a variety of novel 2D vdW epitaxy heterostructures constructed beyond TMDs, however, it has been rarely reported [26].

In the present work, we report a two-step CVD growth method for creating 2D vertically-stacked heterostructure consisting of In_2Se_3 and $MoSe_2$. In_2Se_3, as a III−VI compound semiconductor, has excellent properties for electronic and optoelectronic devices. Recently, the photodetectors of In_2Se_3 with ultrahigh responsivity [29] and tunable near-UV behavior [30] have

*Authors to whom correspondence should be addressed. E-mail: npan@ustc.edu.cn, xpwang@ustc.edu.cn

been reported. $MoSe_2$ is an ideal choice not only for its direct band gap (∼1.5 eV) and strong optical absorption due to band nesting [31], but also for the fact that it is unable to form element doping in In_2Se_3. To our best knowledge, this is the first report of vertically-stacked 2D $In_2Se_3/MoSe_2$ heterostructures obtained by vdW epitaxial growth. The vertical heterostructures were verified by the characterizations of atomic force microscopy (AFM) and Raman spectroscopy. The investigation of transmission electron microscopy (TEM) reveals the well-aligned lattice orientation between In_2Se_3 and $MoSe_2$. In addition, owing to the interlayer interaction, the apparent quenching and small red shift of the photoluminescence (PL) can be observed. More importantly, due to the unique band alignment of the two different materials, the fabricated device exhibits both the current rectification behavior and the photovoltaic effect. The surface contact potential difference of the heterostructure is further characterized by using Kevin probe force microscopy (KPFM).

II. EXPERIMENTS

A. Materials synthesis

$In_2Se_3/MoSe_2$ heterostructures were grown through a two-step CVD process. The experimental set-up is ahown in FIG. 1(a). In the first step, monolayer $MoSe_2$ nanosheets were synthesized on a clean SiO_2/Si substrate in a two-zone furnace. 200 mg selenium (Se) and 10 mg molybdenum oxide (MoO_3) powder were used as precursors and put into a quartz boat and an alumina boat, respectively. They were then pushed into a quartz tube with one inch diameter. Se and MoO_3 quartz tubes were at the center of the first heating zone (zone-1) and the second heating zone (zone-2) respectively. These two heating zones can be controlled separately and the distance between two sources is 23 cm. The SiO_2/Si substrate was put up-side down with the polished side facing towards MoO_3 powder, which located at the bottom of the crucible. The vertical distance between MoO_3 powder and SiO_2/Si substrate is about 0.5 cm. It took 15 min for zone-1 and zone-2 to heat up from room temperature to 100 and 780 °C, respectively. Then zone-1 was heated to 270 °C within 5 min and kept for 30 min, meanwhile zone-2 was kept at 780 °C. 40 sccm Ar (started before heating) and 10 sccm H_2 (started when zone-1 was 270 °C) were used as both the carrier gas and reducing atmosphere to promote the reaction. After that, the furnace was cooled down to room temperature rapidly.

In the second step, the substrate with 1L $MoSe_2$ on top was used as a new substrate for the second growth of In_2Se_2, which was also the template for the synthesis of $In_2Se_3/MoSe_2$ heterostructures. 200 mg Se powder and 10 mg In_2O_3 powder were used as the Se and In precursors. Heating time and carrier gas were kept the same as the growth conditions for $MoSe_2$, but the temperature of zone-2 was reduced to 660 °C and kept for 25 min. All reaction processes are carried out under atmospheric pressure.

B. Characterization

The optical images were taken by optical microscopy (Olympus BX53F). AFM and KPFM were performed using Bruker Demension Icon in the ambient condition. Raman and confocal PL measurements were realized using LabRAM HR 800 under 514 nm excitation. PL mapping measurements was performed with a home-built micro-PL setup. In order to ensure the exciting area to be large enough to cover the whole selected mapping region, 532 nm laser was focused on the back focal plane of objective lens (Olympus M Plan Semi Apochromat, 100×, N.A. 0.9, W.D. 1.0 mm). With a tube lens (300 mm focal length) and long wave pass filter at 550 nm, the luminescence image was enlarged and projected on the slit plane of spectrometer (Princeton Instruments SP2300 with PyLoN:100). For the luminescence image detecting, the width of the slit is set at 2 mm. The zero order interference image reflected by the grating, as the same as the luminescence image, is detected by the CCD of the spectrometer. The spatial resolution is better than 1 μm. For the spectra measurement, the target y direction cut line of the luminescence image was set at the center of the CCD through tuning the x position of the tube lens. Then the width of the slit was set as 50 μm. The cut line spectra, the first order interference image reflected by the grating, are detected by the CCD. The spectrum resolution is better than 0.5 nm, and spatial resolution equals to that of the luminescence image.

TEM, HRTEM images and SAED patterns were collected by a JEOL ARM-200F field emission transmission electron microscope operated at 200 kV. The samples for TEM analyses were transferred onto copper grids coated with 5-nm-thick amorphous carbon film. For sample transfer, polymethylmethacrylate (PMMA, 495A4) was spin-coated on the SiO_2/Si substrate with $In_2Se_3/MoSe_2$ heterostructures at 3000 r/min for 60 s, followed by baking at 120 °C for 3 min to remove the solvents. Then the substrate was floated on 1 mol/L NaOH solution and the PMMA layer carrying samples would shed off the SiO_2/Si substrate slowly. After that, the PMMA film was transferred to deionized water to remove residual ion and then spread onto the copper grid. Finally, the PMMA mediator was removed by dipping in acetone for 3 h.

C. Device fabrication and measurements

The SiO_2/Si substrate with $In_2Se_3/MoSe_2$ heterostructures was spin coated with PMMA (495A4) resist at 3000 r/min for 60 s followed by a 180 °C bak-

DOI:10.1063/1674-0068/30/cjcp1704063

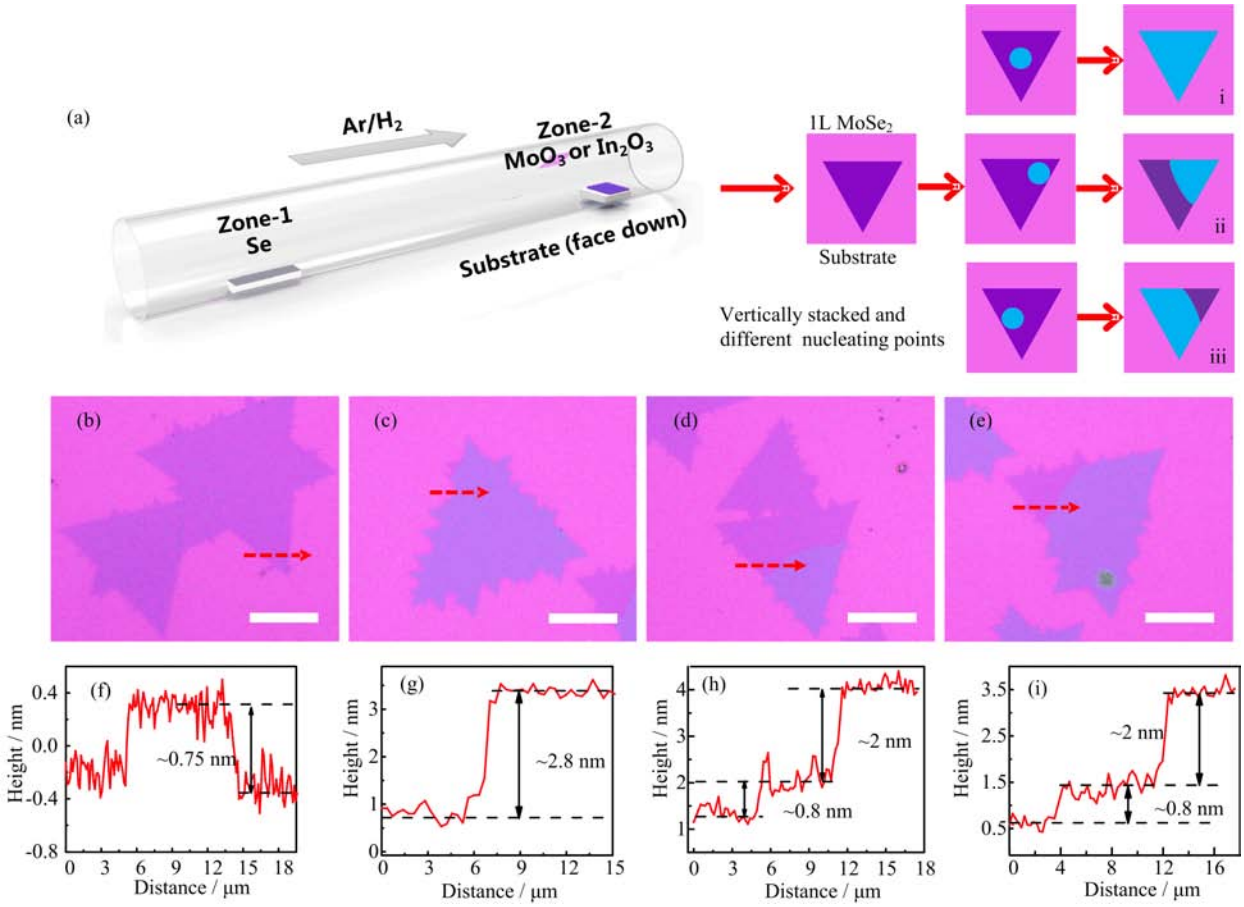

FIG. 1 (a) Schematic of experimental setup for the two step growth of 1L $MoSe_2$ and $In_2Se_3/MoSe_2$ heterostructures (left), and three kinds of growth process of In_2Se_3 sheets on $MoSe_2$ (right). (b) Optical images of the obtained triangular 1L $MoSe_2$ on SiO_2/Si substrate after the first step growth. Scale bar: 20 μm. (c−e) Different types of $In_2Se_3/MoSe_2$ heterostructures after the second step growth, *i.e.*, 1L $MoSe_2$ can be fully covered (c), one-side-uncovered (d) and one-corner-uncovered (e) by In_2Se_3, respectively. Scale bar: 20 μm. (f−i) AFM height profiles along the red dash lines from left to right in (b−e) respectively. The $MoSe_2$ with the thickness of ∼0.75 nm is monolayer (f) and all of the three $In_2Se_3/MoSe_2$ heterostructures contain 2 nm thick (bilayer) In_2Se_3 (g−i).

ing for 90 s. Then the EBL (JEOL, JBX 6300FS) was used to pattern the source and the drain. After development, 5 nm Ti and 50 nm Au contacts were deposited by electron beam evaporation. Lift-off process with acetone finally removed excess metal. The electrical and optoelectronic performance of fabricated device were measured in a Lake Shore CRX-4K probe station ($\sim 10^{-4}$ Pa) with Keithley 4200S semiconductor parameter analyzer. A 532 nm laser with a power density of ~ 0.5 mW/cm^2 was used as the excitation light.

III. RESULTS AND DISCUSSION

FIG. 1(b) shows the results after the first step growth. As seen, triangular $MoSe_2$ flakes with size about several tens of microns can be found clearly. The thickness of the flake is estimated to be ∼0.75 nm by AFM (FIG. 1(f)), indicating that monolayer $MoSe_2$ has been successfully fabricated after the first step CVD process.

After the second CVD process, it is easy to find from FIG. 1(c−e) that the optical contrast of some $MoSe_2$ flakes becomes different, implying that an additional layered material has been grown vertically on the 1L $MoSe_2$. The material can be well identified to be In_2Se_3 using TEM characterization and Raman spectra (see following paragraphs). Further AFM characterization reveals that the thickness of In_2Se_3 is about 2 nm, corresponding to bilayer (FIG. 1(g−i)). Therefore, we can conclude that In_2Se_3(bilayer)/$MoSe_2$(monolayer) heterostructure has been successfully produced by the two-step CVD process. To our best knowledge, this is the first report of direct growth of 2D In_2Se_3 on top of 1L $MoSe_2$ to form the vertically-stacked $In_2Se_3/MoSe_2$ heterostructures.

After carefully examining the optical images of produced heterostructures on the whole substrate, we can classify them into three different kinds of morphologies. The representative results are presented in FIG. 1(c−e).

DOI:10.1063/1674-0068/30/cjcp1704063

The first type is the triangular 1L $MoSe_2$ fullycovered by In_2Se_3 (FIG. 1(c)), the second is $MoSe_2$ partially covered by In_2Se_3 flakes with one side uncovered (FIG. 1(d)), and the third is that with a corner of $MoSe_2$ uncovered (FIG. 1(e)). Moreover, we can find that the edge of In_2Se_3 flake on the top of $MoSe_2$ is rather smooth (FIG. 1(d,e)), hinting that the In_2Se_3 is unlikely formed from the coalescence of several small flakes but most probably grows up from a single seed. Considering In_2Se_3 nucleated randomly on the top of $MoSe_2$, we propose three possible growth processes to reach the experimental results, the schematic is shown in the right of FIG. 1(a). When the nucleation is quite near the center of the single crystal $MoSe_2$, the In_2Se_3 flake tends to fully cover the $MoSe_2$ (type i); when the nucleation is close to one apex of the triangular $MoSe_2$, the In_2Se_3 flake can partially cover the $MoSe_2$ and leave one side uncovered (type ii); similarly, a corner of the $MoSe_2$ will remain uncovered when the In_2Se_3 nucleates around one side of $MoSe_2$ (type iii).

As to the $In_2Se_3/MoSe_2$ heterostructure fabricated on SiO_2 substrate, several issues should be noted. First, monolayer In_2Se_3 can be hardly observed on 1L $MoSe_2$, probably because it is unstable under our growth condition. Second, the thickness of In_2Se_3 flakes can be controlled by tuning the vertical distance between the In_2O_3 source and the substrate as well as the deposition time, therefore different In_2Se_3(multilayer)/$MoSe_2$(monolayer) heterostructure can be produced (FIG. S1(c) in supplementary materials). Third, the $MoSe_2/In_2Se_3$ heterostructure, *i.e.*, $MoSe_2$ on the top of In_2Se_3, cannot be produced on SiO_2 substrate. This is because that In_2Se_3 can hardly nucleate and grow on SiO_2 substrate directly, due to the unsaturated dangling bonds on the surface of SiO_2 and the large lattice mismatch [4] (FIG. S1(a) in supplementary materials). The result is well consistent with the observation shown in FIG. 1(c−e), in which no individual In_2Se_3 flake can be found on the SiO_2 substrate, except on the monolayer $MoSe_2$. Similar to $MoSe_2$, mica also has no unsaturated dangling bonds on its surface, making it an ideal platform for the deposition of In_2Se_3 nanofilms (FIG. S1(b) in supplementary materials).

In order to investigate the crystal quality of the heterostructure and the structure relationship between the In_2Se_3 and the $MoSe_2$, TEM as well as the selected area electron diffraction (SAED) characterizations were carried out on the boundary of $In_2Se_3/MoSe_2$ heterostructure. The heterostructures were transferred from SiO_2/Si substrate to the copper grid with carbon film via traditional PMMA assisted method [32]. FIG. 2(a) shows a low-magnification image focused on the area where 1L $MoSe_2$ is not completely covered by In_2Se_3 (the right part of the white dash line). FIG. 2(b) is the high-resolution TEM image taken from the white line box in FIG. 2(a). As seen, the left region of $MoSe_2$ uncovered by In_2Se_3 demonstrates brighter contrast, while the heterostructure on the right region shows darker contrast. Moreover, the crystal lattice of the heterostructre can be clearly observed, indicating its high crystal quality.

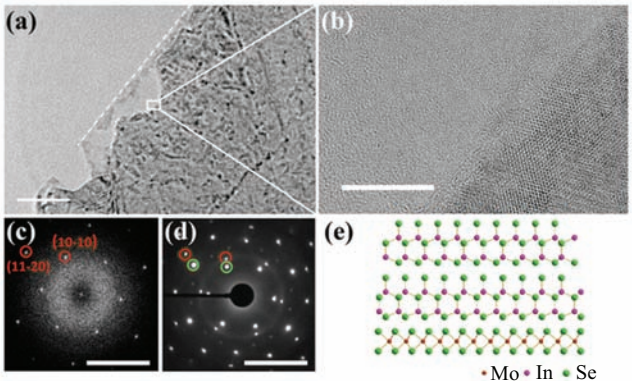

FIG. 2 Structural characterization of the vertically-stacked $In_2Se_3/MoSe_2$ heterostructure. (a) Low magnification TEM image of the edge area where In_2Se_3 is grown on 1L $MoSe_2$. Scale bar: 100 nm. (b) The high-resolution TEM image taken from the white box area marked in (a). Scale bar: 10 nm. (c) Fast Fourier transform (FFT) and (d) the The electron diffraction patterns taken from the left ($MoSe_2$) and right (heterostructure) regions in (b), respectively. Scale bar: 5 nm. The two red circles in (c) and (d) stand for the atomic spacing along [10-10] and [11-20] directions of 2H-$MoSe_2$, whereas the green circles in (d) stand for the atomic spacing along [10-10] and [11-20] directions of α-In_2Se_3. (e) Side view of the atomic model of the $In_2Se_3/MoSe_2$ vertical vdW heterostructure.

The structures of the monolayer $MoSe_2$ and the $In_2Se_3/MoSe_2$ heterostructure are further analyzed by fast Fourier transform (FFT) and SAED. The results taken from the left/right region of FIG. 2(b) are presented in FIG. 2 (c) and (d), respectively. Obviously, typical six-fold diffraction patterns were obtained from both single $MoSe_2$ (left region) and $In_2Se_3/MoSe_2$ heterostructure (right region), consistent with the anticipation of 2H-$MoSe_2$ and α-In_2Se_3. The FFT pattern of $MoSe_2$ in FIG. 2(c) reveals that the probing beam is roughly parallel to c axis of the crystal. The two red circles in the image represent atomic spacing along [10-10] and [11-20] directions, and the corresponding lattice constants were calculated to be 0.28 and 0.16 nm, respectively. These values are in good agreement with the lattice structure of 2H-$MoSe_2$ [26]. The SAED from the heterostructure (FIG. 2(d)) demonstrates two sets of patterns with six-fold symmetry. Compared with FIG. 2(c), we attribute that the spots marked with red circles also come from $MoSe_2$, and the spots marked with green circles are originated from In_2Se_3. We can further acquire information of the crystal structure of In_2Se_3 from the set of green circles. The atomic spacing along the [10-10] and [11-20] directions were calculated to be 0.36 and 0.20 nm, respectively, consistent with the lattice structure of α-In_2Se_3 [29]. More importantly, considering the consistency of the crystal orientation of $MoSe_2$

DOI:10.1063/1674-0068/30/cjcp1704063

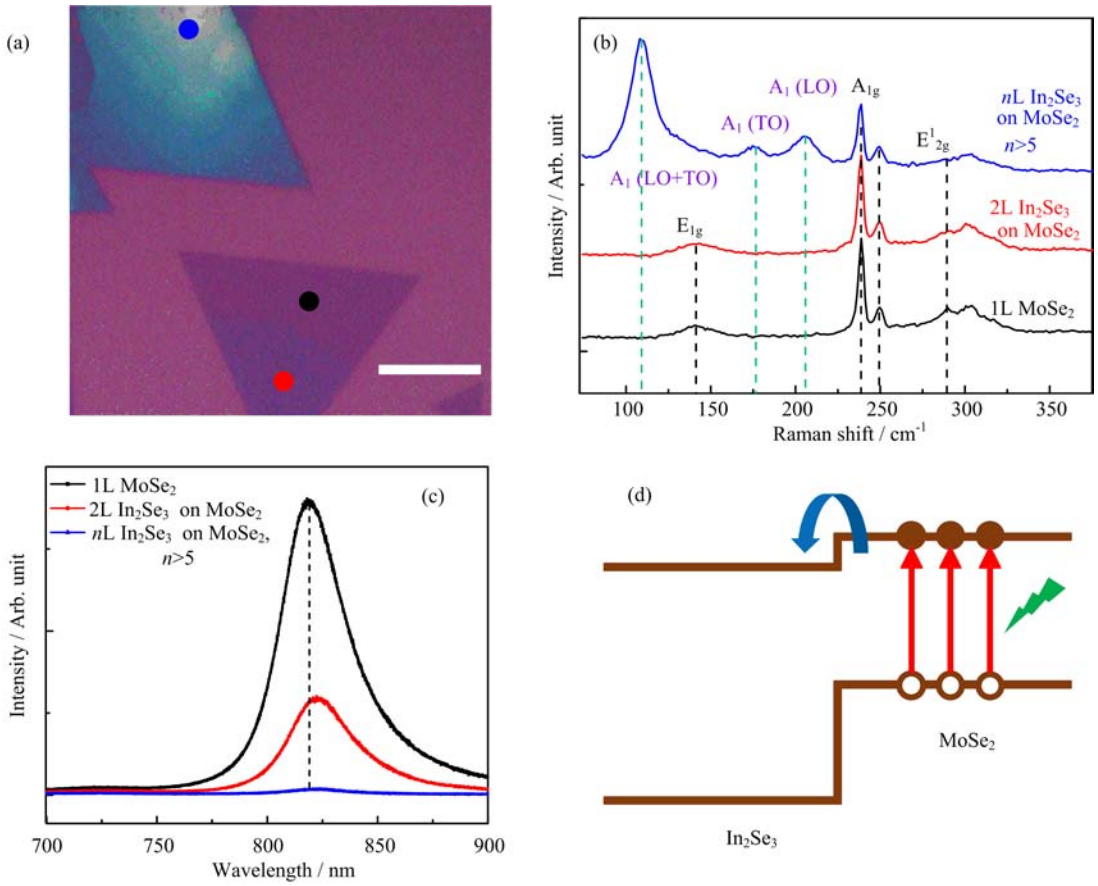

FIG. 3 Optical properties of $In_2Se_3/MoSe_2$ heterostructures. (a) Optical image of heterostructures grown on SiO_2/Si. Scale bar: 10 μm. (b) Raman and (c) PL spectra acquired from the three different points marked in (a), 1L $MoSe_2$ (black point), 2L In_2Se_3 on 1L $MoSe_2$ (red point) and nL In_2Se_3 on 1L $MoSe_2$ (n>5, blue point). (d) Schematic band structure of $In_2Se_3/MoSe_2$.

and In_2Se_3, we consider that 2D α-In_2Se_3 with hexagonal lattice structure has been successfully grown on the top of monolayer $MoSe_2$ by vertical vdW epitaxy. According to the above characterizations, a schematic side view of the atomic model of the $In_2Se_3/MoSe_2$ vdW heterostructure can be roughly depicted in FIG. 2(e).

The optical properties of the vertically stacked $In_2Se_3/MoSe_2$ heterostructures were characterized by Raman and photoluminescence (PL) spectroscopy. The excitation is a 514-nm laser with ∼1 μm spot size. FIG. 3(a) shows the optical image of the heterostructures grown on SiO_2/Si substrate. Three different positions involving bare 1L $MoSe_2$ (black dot), 2L In_2Se_3 on 1L $MoSe_2$ (red point) and nL In_2Se_3 on 1L $MoSe_2$ (n>5, blue point) were excited, and the results of Raman and PL spectra are demonstrated in FIG. 3 (b) and (c), respectively. As seen in FIG. 3(b), for the heterostructure of In_2Se_3(>5 layers)/$MoSe_2$, both Raman peaks from In_2Se_3 and $MoSe_2$ can be observed clearly. Three peaks located at ∼109, ∼177, and ∼206 cm^{-1} (indicated by green dash lines in FIG. 3(b)), can be ascribed to A_1(LO+TO), A_1(TO), and A_1(LO) phonon modes in α-In_2Se_3, respectively [4]. However, because ultrathin In_2Se_3 can be easily damaged even under low-power laser illumination [4], the Raman signal from In_2Se_3 is absent for the 2L $In_2Se_3/MoSe_2$ heterostructure. The rest four Raman peaks, marked by black dash lines, originate from 2H-$MoSe_2$ for ∼141 cm^{-1} (weak E_{1g} mode, in-plane), ∼239 cm^{-1} (A_{1g} mode, out-of-plane), ∼289 cm^{-1} (weak E^1_{2g} mode, in-plane), and ∼250 cm^{-1} (defective peak) [26]. With increasing the In_2Se_3 thickness on the top of $MoSe_2$, the Raman signals of In_2Se_3 increase obviously while the Raman intensities of $MoSe_2$ slightly decrease (especially for the A_{1g} and E^1_{2g} modes). Moreover, we find that the Raman peak positions of monolayer $MoSe_2$ are independent of the thickness of In_2Se_3 flake on top.

FIG. 3(c) shows the PL spectra from monolayer $MoSe_2$ and $In_2Se_3/MoSe_2$ heterostructure. As seen, the maximal PL intensity is obtained in monolayer $MoSe_2$ (black line spectrum in FIG. 3(c)), thanks to its direct band gap [33]. The peak position of PL is approximately at ∼820 nm. For the In_2Se_3(2L)/$MoSe_2$ (1L) heterostructure (red line spectrum in FIG. 3(c)), the PL spectrum shows not only the decrease of intensity

DOI:10.1063/1674-0068/30/cjcp1704063

but also the red shift of peak position to ∼825 nm. The behaviors can be further confirmed by the PL mappings of 1L $MoSe_2$ and In_2Se_3(2L)/$MoSe_2$(1L) heterostructure (FIG. S2 in supplementary materials). Because the bilayer In_2Se_3 owns a too large indirect band gap (∼2.8 eV) to absorb the excitation laser [30], we attribute the predominant reason for the decrease of PL intensity of the heterostructure to the type-II band alignment between 2L In_2Se_3 and 1L $MoSe_2$, as shown in FIG. 3(d). This zigzag band structure is prone to quench the excitons and promote the charge separation, leading to the distinct decrease of photoluminescence [5].

It is found that the full width at half maximum (FWHM) of PL spectra shown in FIG. 3(c) are rather large, which might be caused by the co-existed neutral exciton and trion emissions. In this context, the spectra can be well fitted by two Gaussian functions with neutral exciton (X^0≈818 nm, 1.52 eV) and negative trion (X^-≈834 nm, 1.49 eV). The results are shown in FIG. S3 (supplementary materials) with the red and green lines, respectively. The evaluated trion binding energy ∼30 meV agrees well with previous report [34]. The integrated intensity ratios of negative trion to neutral exciton is found to increase from ∼1.0 for monolayer $MoSe_2$ (FIG. S3(a) in supplementary materials) to ∼1.3 for In_2Se_3(2L)/$MoSe_2$(1L) heterostructure (FIG. S3(b) in supplementary materials). The dominant negative trion emission in the heterostructure implies that the electrons tend to transfer from In_2Se_3 to $MoSe_2$, leading to more negative charge doping in $MoSe_2$ [35]. The result can also account for the PL red shift of the heterostructure in FIG. 3(c).

As to the In_2Se_3(>5L)/$MoSe_2$(1L) heterostructure, PL emission can hardly be found as shown in FIG. 3(c) with blue line. We proposed two causes for the result. One is the exciton quenching effect, which is similar to that observed in the In_2Se_3(2L)/$MoSe_2$(1L) heterostructure. The other is that the optical band gap of In_2Se_3 decreases rapidly with the thickness (∼2.2 eV in 5.5 nm thick In_2Se_3 and 1.45 eV in bulk In_2Se_3) and can even transform into a direct band gap [30], resulting in the strong absorption to the excitation light and weakening the emission.

To investigate the electrical properties of the In_2Se_3/$MoSe_2$ heterostructures, the source-drain contacts consisting of Ti/Au (5/50 nm) were deposited on 2L In_2Se_3/$MoSe_2$ and 1L $MoSe_2$ regions, respectively. The final device is shown in FIG. 4(a) and the schematic structure of the device is shown in the inset. The transfer characteristic of the device shows apparent n-type feature (inset of FIG. 4(b)). This is due to that both $MoSe_2$ and In_2Se_3 are inclined to be intrinsic n-doping during the growth [33, 36]. The I_{ds}-V_{ds} curves under different back-gate voltages ranging from 0 V to 60 V clearly show rectification behavior (FIG. 4(b)), and the rectification ratio can reach as high as ∼100 when V_g<40 V. We attribute the behavior to the n^+-n heterojunction formed between In_2Se_3 and $MoSe_2$, because both materials are n-type semiconductor. The interpretation can be further verified by the fact that the rectification behavior is degraded as V_g becoming large. For instance, the rectification ratio is only ∼5 when V_g≈60 V, as shown in FIG. 4(b).

In order to investigate the band alignment of the heterostructure and identify the proposed n^+-n heterojunction, Kelvin probe force microscope (KPFM) measurement was performed along the red arrow line depicted in FIG. 4(a). As observed from FIG. 4(c), the surface contact potential difference (CPD) across the edge of monolayer $MoSe_2$ and heterostructure can reach ∼200 meV and the width of depletion region is about 4 μm. Because KPFM measures the CPD between the AFM tip and the surface of sample, *i.e.*, $CPD_{sample}=\phi_{tip}-\phi_{sample}$, we can get the Fermi level difference between In_2Se_3 and $MoSe_2$ by:

$$\begin{aligned}\Delta E_F &= E_{F(In_2Se_3)} - E_{F(MoSe_2)} \\ &= \phi_{MoSe_2} - \phi_{In_2Se_3} \\ &= CPD_{In_2Se_3} - CPD_{MoSe_2}\end{aligned} \quad (1)$$

where ϕ_{MoSe_2} and $\phi_{In_2Se_3}$ are the work functions of $MoSe_2$ and In_2Se_3, respectively [37]. Therefore, the value of ΔE_F between In_2Se_3 and $MoSe_2$ can be estimated at ∼200 meV and the band alignment of 2L In_2Se_3 and monolayer $MoSe_2$ is schematically demonstrated in FIG. 4(d). As seen, compared to n-type $MoSe_2$, In_2Se_3 is heavily n-doped semiconductor. Consequently, the In_2Se_3 and $MoSe_2$ can form n^+-n heterojunction, which is the predominant cause for the rectification behavior in FIG. 4(b).

Finally, we present the primary results for the photoresponse of the devices under light illumination. A 532 nm laser with a power density of ∼0.5 mW/cm^2 was used as the excitation light. The I_{ds}-V_{ds} curves of the device with and without light are demonstrated in FIG. S4 in supplementary materials. It can be found that the current increases dramatically with light on. The feature is more striking for the reverse biased device. Specifically, when the device under reverse bias, the current switching ratio of the device with light on to that with light off can be as high as ∼200. However, it decreases to ∼4 for the forward biased device. This phenomenon can be well understood with the band structure of the junction shown in FIG. S4(b) and FIG. S4(c) in supplementary materials. Under the reverse bias (FIG. S4(b) in supplementary materials), in addition to weak dark current, the large band offset can promote the separation of excitons in $MoSe_2$, leading to a high switching ratio; on the contrary, the small band offset under the forward bias voltage (FIG. S4(c)) enables large dark current and therefore lowers the switching ratio. This is similar to the operating principle of p-n photodiode, which further convince the n^+-n band alignment across the In_2Se_3/$MoSe_2$ junction. Additionally, we also observe photovoltaic effect in such a n^+-n heterojunction device. As shown in the inset of

DOI:10.1063/1674-0068/30/cjcp1704063

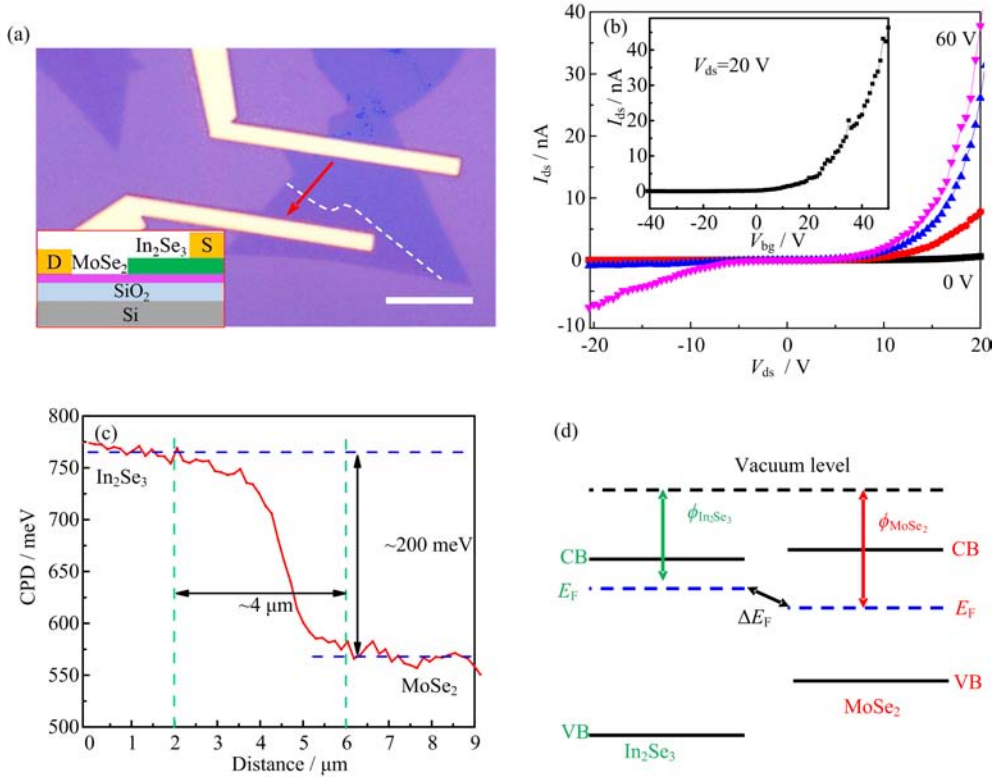

FIG. 4 Electrical characterization of the $In_2Se_3/MoSe_2$ heterostructure. (a) Optical image of a device. The inset is the schematic structure of the device. Scale bar: 10 μm. (b) I_{ds}-V_{ds} curves of the device at different back-gate voltages under dark (from bottom to top, in steps of 20 V). The inset is the transfer characteristic curve with V_{ds} fixed at 20 V. (c) Surface contact potential difference measured along the red arrow line depicted in (a). (d) Band alignment of monolayer $MoSe_2$ and bilayer In_2Se_3 based on KPFM characterization.

FIG. S4 in supplementary materials, the device shows an open-circuit voltage V_{OC}≈0.5 V and short-circuit current I_{SC}≈0.8 pA under light illumination.

IV. CONCLUSION

In summary, we fabricated the vertical heterostructures with bilayer In_2Se_3 on the top of monolayer $MoSe_2$ through a two-step CVD process. The vdW epitaxial character and the possible growth schematic are revealed by the structural characterization. It is found that the quenching behavior and red-shift of photoluminescence of the heterostructure can be modulated by the interaction between $MoSe_2$ and In_2Se_3. Due to the uniquely aligned band structure, such $In_2Se_3/MoSe_2$ heterostructures can exhibit distinct current rectification behavior and photoelectric response. More importantly, the reported approach in this work can be extended to other novel 2D heterostructures involving different layered compounds, enabling to enrich the variety of 2D vdW heterostructures for basic research and applications for next generation optoelectronic devices.

Supplementary materials: More optical micrographs about the growth of In_2Se_3. PL mappings of intrinsic 1L $MoSe_2$ and heterostructure with 1L $MoSe_2$ partially covered by 2L In_2Se_3. Fitted PL spectra of the monolayer $MoSe_2$ and In_2Se_3(2L)/$MoSe_2$ heterostructure. Optoelectronic properties of the $In_2Se_3/MoSe_2$ heterostructure.

V. ACKNOWLEDGMENTS

This work was supported by the Ministry of Science and Technology of China (No.2016YFA0200602), the National Natural Science Foundation of China (No.21421063, No.11374274, No.11404314, No.11474260, No.11504364), the Chinese Academy of Sciences (XDB01020200), and the Fundamental Research Funds for the Central Universities (WK2030020027, WK2060190027).

[1] S. Z. Butler, S. M. Hollen, L. Y. Cao, Y. Cui, J. A. Gupta, H. R. Gutiérrez, T. F. Heinz, S. S. Hong, J. X. Huang, A. F. Ismach, E. Johnston-Halperin, M. Kuno, V. V. Plashnitsa, R. D. Robinson, R. S. Ruoff, S. Salahuddin, J. Shan, L. Shi, M. G. Spencer, M. Terrones, W. Windl, and J. E. Goldberger, ACS Nano **7**, 2898 (2013).

[2] B. Radisavljevic, A. Radenovic, J. Brivio, V. Giacometti, and A. Kis, Nat. Nanotechnol. **6**, 147 (2011).
[3] X. F. Li, M. W. Lin, A. A. Puretzky, J. C. Idrobo, C. Ma, M. F. Chi, M. Yoon, C. M. Rouleau, I. I. Kravchenko, D. B. Geohegan, and K. Xiao, Sci. Rep. **4**, 5497 (2014).
[4] W. Feng, W. Zheng, F. Gao, X. S. Chen, G. B. Liu, T. Hasan, W. W. Cao, and P. A. Hu, Chem. Mater. **28**, 4278 (2016).
[5] F. Ceballos, M. Z. Bellus, H. Y. Chiu, and H. Zhao, ACS Nano **8**, 12717 (2014).
[6] P. Rivera, J. R. Schaibley, A. M. Jones, J. S. Ross, S. Wu, G. Aivazian, P. Klement, K. Seyler, G. Clark, N. J. Ghimire, J. Yan, D. G. Mandrus, W. Yao, and X. Xu, Nat. Commun. **6**, 6242 (2015).
[7] P. Rivera, K. L. Seyler, H. Y. Yu, J. R. Schaibley, J. Q. Yan, D. G. Mandrus, W. Yao, and X. D. Xu, Science **351**, 688 (2016).
[8] A. Pospischil, M. M. Furchi, and T. Mueller, Nat. Nanotechnol. **9**, 257 (2014).
[9] J. S. Ross, P. Klement, A. M. Jones, N. J. Ghimire, J. Q. Yan, D. G. Mandrus, T. Taniguchi, K. Watanabe, K. Kitamura, W. Yao, D. H. Cobden, and X. D. Xu, Nat. Nanotechnol. **9**, 268 (2014).
[10] K. N. Zhang, T. N. Zhang, G. H. Cheng, T. X. Li, S. X. Wang, W. Wei, X. H. Zhou, W. W. Yu, Y. Sun, P. Wang, D. Zhang, C. G. Zeng, X. J. Wang, W. D. Hu, H. J. Fan, G. Z. Shen, X. Chen, X. F. Duan, K. Chang, and N. Dai, ACS Nano **10**, 3852 (2016).
[11] S. J. Haigh, A. Gholinia, R. Jalil, S. Romani, L. Britnell, D. C. Elias, K. S. Novoselov, L. A. Ponomarenko, A. K. Geim, and R. Gorbachev, Nat. Mater. **11**, 764 (2012).
[12] W. Yang, G. R. Chen, Z. W. Shi, C. C. Liu, L. C. Zhang, G. B. Xie, M. Cheng, D. M. Wang, R. Yang, D. X. Shi, K. Watanabe, T. Taniguchi, Y. G. Yao, Y. B. Zhang, and G. Y. Zhang, Nat. Mater. **12**, 792 (2013).
[13] A. K. Geim and I. V. Grigorieva, Nature **499**, 419 (2013).
[14] R. Cheng, D. H. Li, H. L. Zhou, C. Wang, A. X. Yin, S. Jiang, Y. Liu, Y. Chen, Y. Huang, and X. F. Duan, Nano Lett. **14**, 5590 (2014).
[15] M. H. Chiu, C. D. Zhang, H. W. Shiu, C. P. Chuu, C. H. Chen, C. Y. S. Chang, C. H. Chen, M. Y. Chou, C. K. Shih, and L. J. Li, Nat. Commun. **6**, 7666 (2015).
[16] H. Fang, C. Battaglia, C. Carraro, S. Nemsak, B. Ozdol, J. S. Kang, H. A. Bechtel, S. B. Desai, F. Kronast, A. A. Unal, G. Conti, C. Conlon, G. K. Palsson, M. C. Martin, A. M. Minor, C. S. Fadley, E. Yablonovitch, R. Maboudian, and A. Javey, Proc. Natl. Acad. Sci. USA. **111**, 6198 (2014).
[17] C. H. Lee, G. H. Lee, A. M. Van Der Zande, W. C. Chen, Y. L. Li, M. Y. Han, X. Cui, G. Arefe, C. Nuckolls, T. F. Heinz, J. Guo, J. Hone, and P. Kim, Nat. Nanotechnol. **9**, 676 (2014).
[18] S. Tongay, W. Fan, J. Kang, J. Park, U. Koldemir, J. Suh, D. S. Narang, K. Liu, J. Ji, J. B. Li, R. Sinclair, and J. Q. Wu, Nano Lett. **14**, 3185 (2014).
[19] F. Withers, O. Del Pozo-Zamudio, A. Mishchenko, A. P. Rooney, A. Gholinia, K. Watanabe, T. Taniguchi, S. J. Haigh, A. K. Geim, A. I. Tartakovskii, and K. S. Novoselov, Nat. Mater. **14**, 301 (2015).
[20] X. D. Duan, C. Wang, J. C. Shaw, R. Cheng, Y. Chen, H. L. Li, X. P. Wu, Y. Tang, Q. L. Zhang, A. L. Pan, J. H. Jiang, R. Q. Yu, Y. Huang, and X. F. Duan, Nat. Nanotechnol. **9**, 1024 (2014).
[21] Y. J. Gong, S. D. Lei, G. L. Ye, B. Li, Y. M. He, K. Keyshar, X. Zhang, Q. Z. Wang, J. Lou, Z. Liu, R. Vajtai, W. Zhou, and P. M. Ajayan, Nano Lett. **15**, 6135 (2015).
[22] Y. J. Gong, J. H. Lin, X. L. Wang, G. Shi, S. D. Lei, Z. Lin, X. L. Zou, G. L. Ye, R. Vajtai, B. I. Yakobson, H. Terrones, M. Terrones, B. K. Tay, J. Lou, S. T. Pantelides, Z. Liu, W. Zhou, and P. M. Ajayan, Nat. Mater. **13**, 1135 (2014).
[23] H. Heo, J. H. Sung, G. Jin, J. H. Ahn, K. Kim, M. J. Lee, S. Cha, H. Choi, and M. H. Jo, Adv. Mater. **27**, 3803 (2015).
[24] C. M. Huang, S. F. Wu, A. M. Sanchez, J. J. P. Peters, R. Beanland, J. S. Ross, P. Rivera, W. Yao, D. H. Cobden, and X. D. Xu, Nat. Mater. **13**, 1096 (2014).
[25] M. Y. Li, Y. M. Shi, C. C. Cheng, L. S. Lu, Y. C. Lin, H. L. Tang, M. L. Tsai, C. W. Chu, K. H. Wei, J. H. He, W. H. Chang, K. Suenaga, and L. J. Li, Science **349**, 524 (2015).
[26] X. F. Li, M. W. Lin, J. H. Lin, B. Huang, A. A. Puretzky, C. Ma, K. Wang, W. Zhou, S. T. Pantelides, M. F. Chi, K. Kravchenko, J. Fowlkes, C. M. Rouleau, D. B. Geohegan, and K. Xiao, Sci. Adv. **2**, e1501882 (2016).
[27] L. Liu, J. Park, D. A. Siegel, K. F. McCarty, K. W. Clark, W. Deng, L. Basile, J. C. Idrobo, A. P. Li, and G. Gu, Science **343**, 163 (2014).
[28] Y. F. Yu, S. Hu, L. Q. Su, L. J. Huang, Y. Liu, Z. H. Jin, A. A. Purezky, D. B. Geohegan, K. W. Kim, Y. Zhang, and L. Y. Cao, Nano Lett. **15**, 486 (2015).
[29] R. B. Jacobs-Gedrim, M. Shanmugam, N. Jain, C. A. Durcan, M. T. Murphy, T. M. Murray, R. J. Matyi, R. L. Moorell, and B. Yu, ACS Nano **8**, 514 (2014).
[30] J. Quereda, R. Biele, G. Rubio-Bollinger, N. Agraït, R. D'Agosta, and A. Castellanos-Gomez, Adv. Opt. Mater. **4**, 1939 (2016).
[31] A. Carvalho, R. M. Ribeiro, and A. H. C. Neto, Phys. Rev. B **88**, 115205 (2013).
[32] J. Xia, X. Huang, L. Z. Liu, M. Wang, L. Wang, B. Huang, D. D. Zhu, J. J. Li, C. Z. Gu, and X. M. Meng, Nanoscale **6**, 8949 (2014).
[33] Y. J. Gong, G. L. Ye, S. D. Lei, G. Shi, Y. M. He, J. H. Lin, X. Zhang, R. Vajtai, S. T. Pantelides, W. Zhou, B. Li, and P. M. Ajayan, Adv. Funct. Mater. **22**, 2009 (2016).
[34] A. Singh, G. Moody, K. Tran, M. E. Scott, V. Overbeck, G. Berghäuser, J. Schaibley, E. J. Seifert, D. Pleskot, N. M. Gabor, J. Q. Yan, D. G. Mandrus, M. Richter, E. Malic, X. D. Xu, and X. Q. Li, Phys. Rev. B **93**, 041401 (2016).
[35] J. S. Ross, S. F. Wu, H. Y. Yu, N. J. Ghimire, A. M. Jones, G. Aivazian, J. Q. Yan, D. G. Mandrus, D. Xiao, W. Yao, and X. D. Xu, arXiv preprint arXiv: 1211.0072, (2012).
[36] M. Lin, D. Wu, Y. Zhou, W. Huang, W. Jiang, W. S. Zheng, S. L. Zhao, C. H. Jin, Y. F. Guo, H. L. Peng, and Z. F. Liu, J. Am. Chem. Soc. **135**, 13274 (2013).
[37] K. Chen, X. Wan, J. X. Wen, W. G. Xie, Z. W. Kang, X. L. Zeng, H. J. Chen, and J. B. Xu, ACS Nano **9**, 9868 (2015).

DOI:10.1063/1674-0068/30/cjcp1704063